AIAA JOURNAL
Vol. 32, No. 11, November 1994

Adaptive Finite Element Method for Turbulent Flow near a Propeller

Dominique Pelletier,* Florin Ilinca,† and Jean-François Hétu‡
CERCA and École Polytechnique de Montréal, Montréal, Quebec H3C 3A7, Canada

This paper presents an adaptive finite element method based on remeshing to solve incompressible turbulent free shear flow near a propeller. Solutions are obtained in primitive variables using a highly accurate finite element approximation on unstructured grids. Turbulence is modeled by a mixing length formulation. Two general purpose error estimators, which take into account swirl and the variation of the eddy viscosity, are presented and applied to the turbulent wake of a propeller. Predictions compare well with experimental measurements. The proposed adaptive scheme is robust, reliable and cost effective.

Nomenclature

e = error
f = body force
h = element size
$J(\bullet)$ = energy functional
L_m = mixing length
$\hat{n}$ = outward unit vector
p = pressure
R = propeller radius
S = torque
T = thrust
$\boldsymbol{u}$ = velocity vector
w = test function
ρ = density
$\dot{\gamma}$ = strain rate tensor
∇ = gradient operator
$\nabla\bullet$ = divergence
μ = viscosity
η = relative error
δ = element size for new mesh

Subscripts

∂,B = boundary
0 = reference value
av = average
ex = exact solution
h = finite element solution
l = laminar
m = maximum
t = turbulent

Introduction

ADAPTIVE finite element methods provide a powerful approach for tackling complex computational fluid dynamics problems. They provide a framework for optimizing several aspects of the computational process. For instance, grid points can be clustered in regions of rapid solution variation to improve accuracy. This is often done in such a way as to result in a uniformly accurate solution throughout the domain. The adaptive process is then cost effective in the sense that the best numerical solution is obtained at the least computational cost. Moreover, such approaches provide flexibility in modeling and algorithm development and can, at least in theory, provide quantitative measures of the accuracy of the solutions computed. The ability of the methodology to produce uniformly accurate solutions makes it possible to obtain numerically exact solutions (grid independent) to the equations of motion, so that mathematical models of the physical phenomenon of interest can be evaluated with confidence.

Initial breakthroughs were achieved in aerodynamics because of the pressing need for accurate computations of shock waves.[1] However, little work has been done for incompressible flows and even less for turbulent flow problems. Proof of concept computations for laminar incompressible flow were reported by Wu et al.[2] and Wang and Cary.[3] In the work of Hétu and Pelletier,[4,5] Pelletier and Hétu,[6] and Pelletier et al.,[7] the methodology proposed by the authors was quantitatively validated by solving laminar flows with known analytical solution and by computing cases for which experimental measurements were available. This paper presents a rigorous extension of the methodology to turbulent free shear flows. The methodology is based on adaptive remeshing coupled to a finite element solver for steady-state incompressible turbulent flows for which turbulence is modelled by a mixing length model.

The paper is organized as follows. First we describe the modeling of the problem. The equations of motion and the finite element solver are reviewed. The turbulence model is discussed and details of the nonlinear equation solver are given. The modeling of the propeller is also presented. The methodology section describes two error estimators and the adaptive remeshing strategy. The proposed methodology is then validated by solving a problem with a known analytical solution to clearly quantify the accuracy improvements due to adaptivity. The method is then applied to free shear flows near a propeller for which experimental data are available. The paper closes with conclusions.

Modeling of the Problem

Equations of Motion

The flow regime of interest is modeled by the Reynolds-averaged Navier-Stokes equations:

$$\rho \boldsymbol{u}\bullet\nabla\boldsymbol{u} = -\nabla p + \nabla\bullet[2\mu\dot{\gamma}(\boldsymbol{u})] + f$$
$$\nabla\bullet\boldsymbol{u} = 0 \tag{1}$$

where μ is the effective viscosity (the sum of the eddy and fluid viscosities) and f are body forces representing the effects of the propeller disk. The strain rate tensor is defined by

$$\dot{\gamma}(\boldsymbol{u}) = (1/2)\{\nabla\boldsymbol{u} + (\nabla\boldsymbol{u})^T\} \tag{2}$$

Received April 12, 1993; presented as Paper 93-2767 at the AIAA 11th Computational Fluid Dynamics Conference, Orlando, FL, July 6–9, 1993; revision received May 3, 1994; accepted for publication May 3, 1994.

*Associate Professor, Mechanical Engineering Department, P.O. Box 6079, Succursale Centre-ville.

†Graduate Research Assistant, Mechanical Engineering Department, P.O. Box 6079, Succursale Centre-ville.

‡Graduate Research Assistant; currently Research Officer, National Research Council of Canada, Institute for Industrial Materials, 75, de Mortagne, Boucherville, Canada.

Appropriate Dirichlet and Newmann boundary conditions complete the statement of the problem:

$$\begin{aligned} \boldsymbol{u} &= \boldsymbol{u}_0 \quad \text{on } \Gamma_u \\ 2\mu\dot{\gamma}(\boldsymbol{u}) \bullet \hat{n} - p\hat{n} &= t^* \quad \text{on } \Gamma_t \end{aligned} \tag{3}$$

where $\hat{n}$ is the outward unit normal vector and t^* a given force acting on the boundary.

The flowfield of interest is axisymmetric; hence the Reynolds-averaged Navier-Stokes equations are written in axisymmetric coordinates. The unknowns are the axial, radial, and swirl velocity components and the pressure.

Turbulence Model

Following Refs. 8–11, turbulence is modeled using Boussinesq's eddy-viscosity concept, which assumes that turbulent stresses are proportional to the mean velocity gradients. Using this hypothesis the effective viscosity may be expressed as

$$\mu = \mu_l + \mu_t \tag{4}$$

where μ_l is the molecular viscosity, and μ_t the turbulent eddy viscosity. To close the equations of motion, the eddy viscosity must be related to the other unknowns of the problem. The flow behind a propeller is very similar to jets and wakes: a velocity excess is present downstream of the thrusting part of the propeller, and a defect is also present near the root and tip of the blade. Hence a mixing length model is appropriate,[11] given by

$$\mu_t = \rho L_m^2 \{ [\nabla \boldsymbol{u} + (\nabla \boldsymbol{u})^T] : \nabla \boldsymbol{u} \}^{1/2} \tag{5}$$

This approach has already proven to be very cost effective.[8,11] The mixing length is taken to be

$$L_m = 0.09\delta \tag{6}$$

where δ is defined as the distance between points such that the velocity differs from the freestream by 10% of the maximum velocity difference across the layer.[11] For symmetric flows, δ is the distance from the axis of symmetry to the 10% point at the outer edge of the free shear layer.[9–11] Since the width of the free shear layer will not vary by much in the near field of the propeller wake, we take δ = 90% of the propeller radius, a choice that has proven adequate in our previous work[9] and was confirmed through computations using another turbulence model.[8] More sophisticated models with variable L_m or using the integrated turbulence kinetic energy equation[8] can be implemented readily in the current code. However, for the present class of free shear flow problems, higher order models such as two-equation models have not been shown to yield much improvement in predictions to warrant the added cost and complexity. The only exception is probably for cases in which freestream turbulence effects play an important role.

Finite Element Solver

The starting point for the finite element solver is the weak Galerkin form of the equations of motion. The momentum and continuity equations (1) are multiplied by an appropriate test function and diffusion terms are integrated by parts over the domain. The resulting variational form is given by

$$\begin{aligned} (\rho u \bullet \nabla \boldsymbol{u}, \boldsymbol{v}) + a(\boldsymbol{u}, \boldsymbol{v}) - (p, \nabla \bullet \boldsymbol{v}) &= (f, \boldsymbol{v}) + \langle t^*, \boldsymbol{v} \rangle \\ (q, \nabla \bullet \boldsymbol{u}) &= 0 \end{aligned} \tag{7}$$

with

$$\begin{aligned} (h, g) &= \int_\Omega hg \, d\Omega \\ a(\boldsymbol{u}, \boldsymbol{v}) &= \int_\Omega 2\mu\dot{\gamma}(\boldsymbol{u}) : \dot{\gamma}(\boldsymbol{v}) \, d\Omega \\ \langle t^*, \boldsymbol{v} \rangle &= \int_{\partial K \setminus \Gamma_t} [2\mu\dot{\gamma}(\boldsymbol{u}) \bullet \hat{n} - p\hat{n}] \bullet \boldsymbol{v} \, ds + \int_{\partial K \cap \Gamma_t} t^* \bullet \boldsymbol{v} \, ds \end{aligned} \tag{8}$$

These variational equations are solved by a standard Galerkin method coupled to an augmented Lagrangian algorithm to treat incompressibility.[4,6,7] Equation (5) for the eddy viscosity introduces strong nonlinearities in the equations of motion. The diffusion terms are linearized with Newton's method and lead to an extra contribution to the finite element matrix:

$$\int_\Omega \rho L_m^2 \frac{2\dot{\gamma}(\boldsymbol{u}) : \dot{\gamma}(\delta \boldsymbol{u})}{\{2\dot{\gamma}(\boldsymbol{u}) : \dot{\gamma}(\boldsymbol{u})\}^{1/2}} \bullet 2\dot{\gamma}(\boldsymbol{u}) : \dot{\gamma}(\boldsymbol{v}) \, d\Omega \tag{9}$$

where $\delta \boldsymbol{u}$ are the Newton corrections for the velocities. The equations are discretized using the seven-node triangular element, which uses an enriched quadratic velocity field and a linear discontinuous pressure.[4,5] This element may appear expensive at first sight. However, it is ideally suited for fully unstructured grids. Such meshes, coupled to an adaptive remeshing strategy, lead to quasioptimal allocation of grid points and result in a overall computationally efficient algorithm as shown at the end of the paper.

Modeling of the Propeller

The present work focuses on the prediction of the turbulent steady-state mean flow in the near wake of the propeller. Only the effect of the propeller on the mean flowfield is needed. Details of the propeller blade interaction with the incoming flow is not required. The jump to trying to treat the three-dimensional cyclically unsteady problem with individual blades with their thin boundary layers and wake is too great to be attempted in one step at this time even though it is of great practical importance. Hence, following Ref. 8, the propeller is modeled by a thin disk of finite thickness whose radius is equal to the propeller radius. The thrust and torque vary in the radial direction. However, since little is known about the radial distribution of thrust and torque, some assumptions must be made. Generally one only knows the global values of thrust and torque. For simplicity we use a trapezoidal distribution that has proved successful in our previous work[8]:

$$\begin{aligned} t(r) &= 0 && r \in [0, r_1] \\ t(r) &= t_m (r - r_1)/(r_2 - r_1) && r \in [r_1, r_2] \\ t(r) &= t_m && r \in [r_2, r_3] \\ t(r) &= t_m (R - r)/(R - r_3) && r \in [r_3, R] \\ t(r) &= 0 && r > R \end{aligned} \tag{10}$$

where t_m is the maximum value of the thrust and R the radius of the propeller. Values of r_1, r_2, and r_3 were set to $0.25R$, $0.7R$, and $0.85R$, respectively. The same form is adopted for the distribution of the tangential force s producing swirl. These distributions are integrated over the volume swept by the propeller to yield the global thrust and torque

$$\begin{aligned} T &= 0.3075 \times 2\pi R^2 t_m \\ S &= 0.2218 \times 2\pi R^3 s_m \end{aligned} \tag{11}$$

The values of t_m and s_m are determined by matching these results with the global values of the thrust and torque coefficients obtained from experiments or from a performance analysis code. The body forces required by the finite element code are obtained by dividing the thrusting and swirling forces by the thickness of the propeller disk. They are thus assumed to be uniform through the thickness of

the disk which is set to 0.041 propeller diameter, a dimension that roughly corresponds to the axial thickness of the propeller used in the experiments.[10] It should be noted that this approach lumps many intricacies of the propeller effects into the body force terms. This is acceptable in the present case since the analysis focuses on the mean flow of the wake. Furthermore, detailed analyses required to answer questions concerning thrust and torque loading of propeller blades would require a fully three-dimensional time dependent computation. Although feasible, it remains a formidable task beyond the scope of the present paper.

Adaptive Methodology

Generalities

The basic idea behind most adaptive methods is to assess the quality of an initial solution obtained on a coarse mesh by using some form of error estimation and to modify the structure of the numerical approximation in a systematic fashion so as to improve the overall quality of the solution. There are several ways of achieving adaptivity: *P* methods increase the degree of the polynomial approximation to improve accuracy[12]; *R* methods relocate grid points[13]; and *H* methods proceed by either mesh enrichment or remeshing.[1,4]

A variant of an *H* method, called adaptive remeshing, has been retained because it provides the greatest control of element size and grading to accurately resolve flow features such as shear layers, jets, and wakes. In this approach, the problem is first solved on a coarse grid to roughly capture the physics of the flow. The resulting solution is then analyzed to determine where more grid points are needed, and an improved mesh is generated. The problem is solved again on the new mesh using the solution obtained on the coarser mesh as an initial guess. This process is repeated until the required level of accuracy is achieved.

Remeshing also offers an elegant and simple approach to overcome some of the obstacles specific to incompressible viscous flows. For instance, the best proven finite element approximations can be selected based on their convergence and accuracy properties.[14,15] This circumvents the problem associated with *P* methods of satisfying the so-called Ladyshenskaya-Bubuska-Brezzi compatibility condition between the velocity and pressure approximations. This condition states that only specific pairs of velocity and pressure interpolants will lead to stable solutions free of checkerboard or parasitic pressures. It also eliminates the "hanging node problem" encountered in some *H*-refinement methods[3] for which special algorithms must be invoked to ensure continuity of the solution and stability of the algorithm.

Error Estimation

This section describes two error estimation techniques for assessing the accuracy of the solutions obtained by the finite element solver.

Projection Error Estimator

This approach was first introduced by Zienkiewicz and Zhu[16] and involves postprocessing of the stresses and strains. For incompressible creeping flows, with constant physical properties, this estimator can be derived from the variational principle for Stokes flow, which consists in finding a velocity vector $\boldsymbol{U}$ that minimizes the dissipation energy

$$J(U) = \int \mu [\nabla U + (\nabla U)^T] : [\nabla U + (\nabla U)^T] \, dx$$

$$= \int 2\sigma : \dot{\gamma} \, dx \tag{12}$$

If U_h and U_{ex} are the approximate and exact solutions respectively, the dissipation energy of the error can be computed by evaluating

$$J(e) = J(U_h - U_{ex}) = \int 2(\sigma_h - \sigma_{ex}) : (\dot{\gamma}_h - \dot{\gamma}_{ex}) \, dx \tag{13}$$

Unfortunately, the exact solution is not available in cases of practical interest. However, it has been shown that the exact stresses and strains can be replaced by a least-squares projection of the finite element stresses and strains σ_h and γ_h in the space of continuous interpolation functions for velocity. Let $\tilde{\sigma}_h$ and $\tilde{\gamma}_h$ denote the required least-squares projection on each element we can write

$$\tilde{\sigma}_h = \sum N_i \tilde{\sigma}_{h_i}$$
$$\tilde{\gamma}_h = \sum N_i \tilde{\gamma}_{h_i} \tag{14}$$

where N_i are the velocity interpolation functions. The nodal values of $\tilde{\sigma}_h$ are obtained by minimizing the following expression:

$$\min \int_\Omega (\tilde{\sigma}_h - \sigma_h)^2 \, d\Omega \tag{15}$$

Differentiation with respect to $\tilde{\sigma}_{h_i}$ leads to the following system of algebraic equations:

$$\left[\int_\Omega N_i N_j\right] \tilde{\sigma}_{h_j} = \int_\Omega N_i \sigma_h \tag{16}$$

which is solved by Gaussian elimination. A similar system is solved for the projection of $\dot{\gamma}_h$. See Refs. 6, 16, and 17 for technical details.

This estimator does not include the effects of pressure. However, it is a simple matter to generalize the estimator to properly treat pressure variations. The pressure approximation being discontinuous, its least-squares projection into the space of velocity interpolation functions is easily computed. The pressure contribution to the error is then given by

$$e_h^p = \tilde{p}_h - p_h \tag{17}$$

where the tilde denotes a least-squares projection.

The combined norm of the velocity and pressure errors is computed as follows:

$$\| (\boldsymbol{u}, p) \| = \{ \| \boldsymbol{u} \|_E^2 + \| p \|_0^2 \}^{1/2} \tag{18}$$

where

$$\| \boldsymbol{u} \|_E = \left\{ \int_\Omega 4\mu^2 \dot{\gamma}(\boldsymbol{u}) : \dot{\gamma}(\boldsymbol{u}) \, d\Omega \right\}^{1/2}$$
$$\| p \|_0 = \left\{ \int_\Omega | p |^2 d\Omega \right\}^{1/2} \tag{19}$$

This is the so-called natural norm induced by the variational formulation of the problem. Incorporation of the pressure term in the error estimator was shown to play a critical role in obtaining accurate predictions in situations where velocity gradients are small and pressure variations control the flow.[5]

Local Variational Problem for the Error

This approach provides estimates of the error without having to solve the global least-squares problems required for the Zhu estimator. Variational equations for the velocity and pressure errors can be derived directly from the Navier-Stokes equations[5,17] by setting $\boldsymbol{u} = \boldsymbol{u}_h + e^u$ and $p = p_h + e^p$ in Eqs. (7). After some rearrangement one obtains

$$a(e^u, v_h) - (e^p, \nabla \cdot v_h) = -a(u, v_h) + (f - \rho \boldsymbol{u}_h \cdot \nabla \boldsymbol{u}_h, v_h)$$
$$(+p_h, \nabla \cdot v_h) + \langle [2\mu\dot{\gamma} \cdot n - p_h n]_A, v_h \rangle_{\partial K \setminus \Gamma_i} + \langle \hat{t}, v_h \rangle_{\partial K \cap \Gamma_i}$$
$$(q_h, \nabla \cdot e_h^u) = (q_h, \nabla \cdot \boldsymbol{u}_h) \tag{20}$$

The terms in parentheses on the right-hand side of Eq. (20) represent the element residual, a measure of the accuracy of the finite

element solution inside an element. The terms in brackets are the average viscous fluxes across element faces. The difference between this average value and the raw fluxes computed on the face of the element reflects how well the solutions on two neighboring elements are matched. The second equation of Eq. (20) is a measure of mass conservation.

This variational problem is discretized locally on each element. Velocity errors are approximated with three quartic bubble functions obtained by squaring the quadratic velocity interpolation associated to midside nodes. The pressure error is approximated with a quadratic bubble function. This results in small 10×10 systems of equations for each element that are inexpensive to solve. The norm of the combined errors is computed using the same norm, Eqs. (18) and (19), used in the projection error estimate. This local problem approach was originally introduced as an economical alternative to the projection method. It turns out that the combination of quartic interpolants for the error and a variable eddy viscosity mandates the use of very high-order Gaussian integration rules to construct the local systems (up to 19 points per triangle). The net result is that the local problem approach is somewhat more expensive than the projection method. However, it is generally more accurate.

Adaptive Remeshing

There remains to discuss how one exploits the knowledge of the error distribution to design a better mesh. The adaptive remeshing strategy is straightforward and follows that proposed in Refs. 1, 4, and 5 and proceeds as follows:

```
1 - Generate an initial mesh
2 - Compute the finite element solution
3 - Compute error estimate
4 - if ( global error < tolerance ) then
        - stop
    else
        - compute element size from error estimate
        - generate an improved mesh according to
          element size distribution
        - interpolate current solution on new mesh
      - goto 2
    end if
```

We now provide details on some of the steps of this algorithm. Once the finite element solution has been obtained, the error on each element is computed using one of the previously described estimators. The global norms of the solution and the error are computed as follows:

$$\| e_{\text{tot}} \|^2 = \sum \| e_k \|^2 \tag{21}$$

so that the relative error can be evaluated as

$$\eta = \| e_{\text{tot}} \| / \| U \| \tag{22}$$

There remains to compute the element size for the improved mesh so that elements are smaller in regions of large error and bigger in regions where the solution is already accurate. This is achieved by requiring that the improved mesh be optimal (i.e., that all elements have the same average error e_{av}). Now, given a target relative error η_t, the total and average error can be related as follows:

$$\| e_{\text{av}} \| = \eta_t \frac{\| U \|}{\sqrt{n}} \tag{23}$$

where n is the number of elements in the mesh.

Finally, an expression for element sizes can be derived from the asymptotic rate of convergence of the finite element approximation which relates the error to some power k of the element size h

$$\| e \| = ch^k \tag{24}$$

where c is an unknown constant. For the seven-node triangle, $k = 2$. This expression can also be written for the target error

$$\| e_{\text{av}} \| = c\delta^k \tag{25}$$

These two equations can be solved for the required element size by eliminating c from Eqs. (24) and (25)

$$\delta = \left[\frac{\eta_r \| U \|}{\| e \| \sqrt{n}} \right]^{1/k} h \tag{26}$$

This distribution of element size is then used in an advancing front mesh generator to generate an improved mesh.

Validation

The two error estimators are first compared on a simple flow problem for which an analytical solution is known. This provides controlled conditions to validate the proposed adaptive strategy and assess its computational performance for swirling flows.

For this problem the analytical solution was taken to be

$$u = 1 - y^2, \qquad v = 0$$

$$w = [\exp(Re^* y) - 1] / [\exp(Re) - 1], \qquad p = x - 0.2$$

The thickness of the boundary layer in the w component is controlled by the Reynolds number Re. In this problem only the swirl velocity field will contribute to the error since the finite element approximation provides an exact representation of the axial velocity and the pressure. The problem is solved on the $[0,0.2] \times [0,1]$ domain. The adaptive strategy is set to reduce the computed error by a factor of three at each cycle. Tables 1 and 2 illustrate the performance of the adaptive strategy for both the projection and local problem error estimators.

As can be seen, both error estimators drive the adaptation process to reduce the error and its estimate at each cycle. Hence the solution accuracy improves steadily at each adaptation cycle. Note also that the local problem approach provides a better estimate of the error than the projection method. Figures 1 and 2 are histograms of the element errors: a count of the number of elements whose error norm falls in a given interval. Observe the sharp peak and tight grouping around the mean value of the error which indicates that a large portion of the elements have nearly the same error. In other words, the adaptive strategy has achieved a nearly op-

Table 1 Projection estimator

Mesh	No. of nodes	No. of elements	Error estimate	True error
0	109	42	2.497×10^{-3}	7.394×10^{-3}
1	119	50	7.739×10^{-4}	1.886×10^{-3}
2	250	111	3.420×10^{-4}	7.132×10^{-4}
3	523	242	1.082×10^{-4}	2.528×10^{-4}
4	1247	592	4.659×10^{-5}	1.060×10^{-4}

Table 2 Local problem estimator

Mesh	No. of nodes	No. of elements	Error estimate	True error
0	109	42	3.607×10^{-3}	7.394×10^{-3}
1	105	42	1.491×10^{-3}	1.922×10^{-3}
2	236	105	6.278×10^{-4}	8.768×10^{-4}
3	500	231	2.016×10^{-4}	2.823×10^{-4}
4	1052	499	9.434×10^{-5}	1.301×10^{-4}

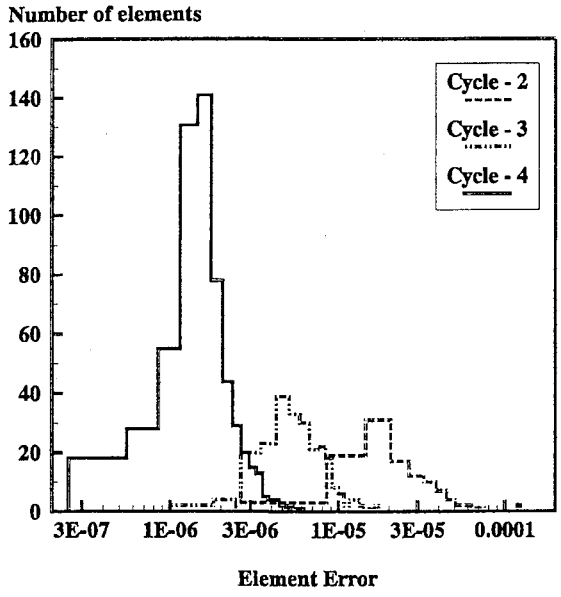

Fig. 1 Error distribution, projection estimator.

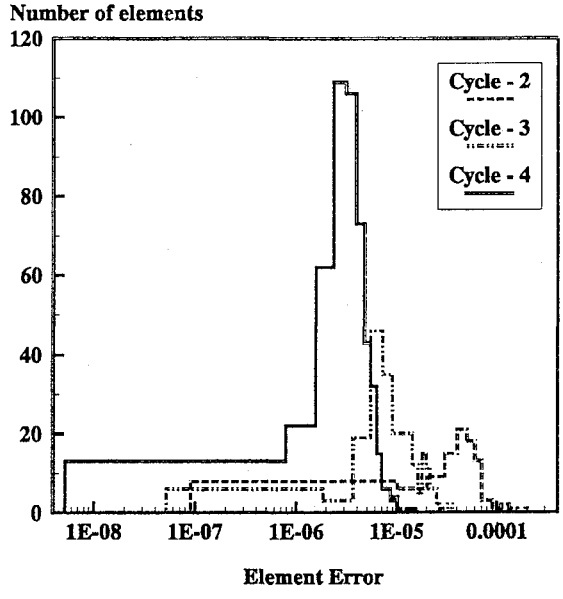

Fig. 2 Error distribution, local problem.

timal mesh. Note that the horizontal scale is logarithmic, so that the low and wide band in Fig. 2 represents 13 elements out of a total of 1052, for which the solution is far more accurate than in other elements.

Results and Discussion

This section presents the application of the two error estimators to uniform turbulent flow past a propeller. The adaptive strategy was set to attempt a reduction of the error by a factor of three at each cycle. The codes were run in a blackbox fashion requiring no user intervention.

Nondimensionalization

All calculations were performed with a nondimensional form of the equations of motion. Reference values are selected for the velocity U_0^*, length L_0^*, and pressure P_0^* to obtain the following dimensionless variables for Eqs. (1–7) (the asterisk denotes a dimensional variable)

$$x_i = \frac{x_i^*}{L_0^*}, \quad u_i = \frac{u_i^*}{U_0^*}, \quad p = \frac{p^* - P_0^*}{\rho^* U_0^{*2}}, \quad \rho = \frac{\rho^*}{\rho_0^*} = 1$$
$$\mu = \frac{\mu^*}{\rho^* U_0^* L_0^*} = \frac{1}{Re}, \quad f = \frac{f^*}{\rho^* U_0^{*2}/L^*} \tag{27}$$

The characteristics of the flow, measured by Kotb,[10] are

$$U_0^* = 8.52 \text{ m/s}, \quad L_0^* = D^* = 0.492 \text{ m}, \quad N = 1150 \text{ rpm}$$
$$\mu_l = 1.8 \times 10^{-5} \text{ kg/(s • m)}, \quad \rho_0^* = 1.179 \text{ kg/m}^3 \tag{28}$$
$$K_T = \frac{T}{\rho_0^* N^2 D^{*4}} = 0.150, \quad K_s = \frac{S}{\rho_0^* N^2 D^{*5}} = 0.0279$$

Modeling and Boundary Conditions

The inflow boundary is located two diameters upstream of the propeller and the outflow plane stands at three diameters downstream of the propeller. The freestream boundary is a cylindrical shell of radius 1.2 diameters. At the inflow, the streamwise velocity u_x is set to unity, and the radial and tangential components u_r and u_θ are set to zero. On the freestream boundary u_x is set to one, and the r and θ tractions are set to zero. The three components of the traction vector are set to zero at the outflow boundary.

A word of caution is in order concerning the accuracy of the predictions and measurements. Firstly, the computation does not include the shaft and drive-train housing of the experiments (Fig. 3). In the experiment a body is placed close to and downstream of the propeller to house the drive train. The housing begins at 0.23 propeller diameter downstream of the disk so that its presence will affect the experimental results from the station located at $x/D = 0.23$ which sits right on the body. One would expect this difference to affect comparison between predictions and measurements. Inclusion of the body would require a fully three-dimensional simula-

Table 3 Projection estimator

Mesh	No. of nodes	No. of elements	Error estimate	Solution norm
0	388	181	4.536×10^{-3}	2.197×10^{-2}
1	623	294	1.634×10^{-3}	2.131×10^{-2}
2	1339	648	6.633×10^{-4}	2.124×10^{-2}
3	3166	1553	2.461×10^{-4}	2.124×10^{-2}
4[a]	5051	2492	1.248×10^{-4}	2.123×10^{-2}

[a]Reduction of the error by a factor of 2.

Table 4 Local problem estimator

Mesh	No. of nodes	No. of elements	Error estimate	Solution norm
0	388	181	1.038×10^{-2}	2.197×10^{-2}
1	643	302	3.011×10^{-3}	2.126×10^{-2}
2	1393	672	1.133×10^{-3}	2.124×10^{-2}
3	2930	1431	4.647×10^{-4}	2.124×10^{-2}
4[a]	4953	2432	1.935×10^{-4}	2.123×10^{-2}

[a]Reduction of the error by a factor of 2.5.

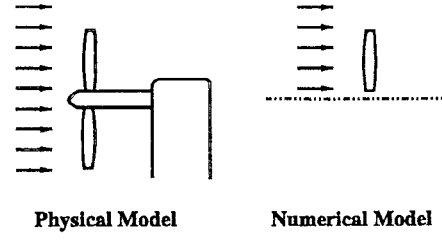

Fig. 3 Experimental and numerical configurations.

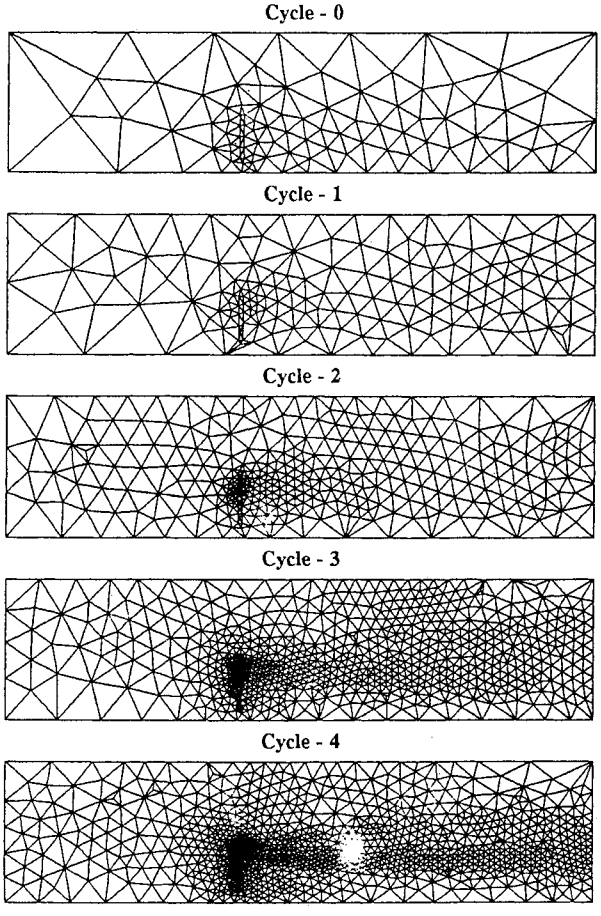

Fig. 4 Initial and adapted meshes.

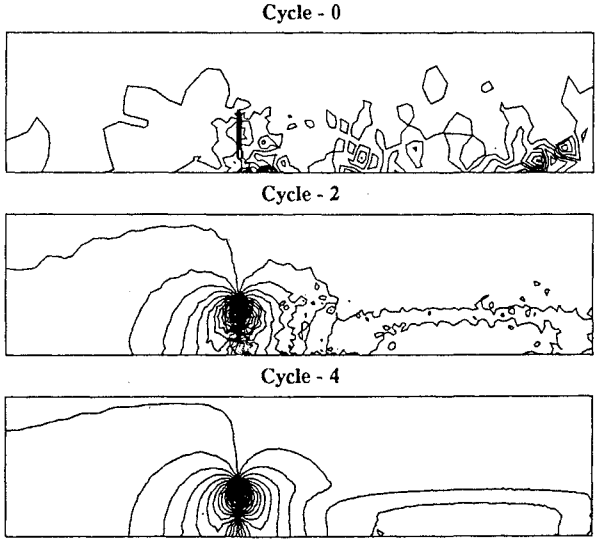

Fig. 5 Pressure contours.

Table 5 Computational statistics for adaptation

Cycle	No. of iters.	Mesh generation, s	Solution, s	Adaptation, s
0	11	0.59	38.47	1.44
1	6	1.78	43.19	2.35
2	5	3.20	99.76	5.33
3	4	7.09	305.64	14.44

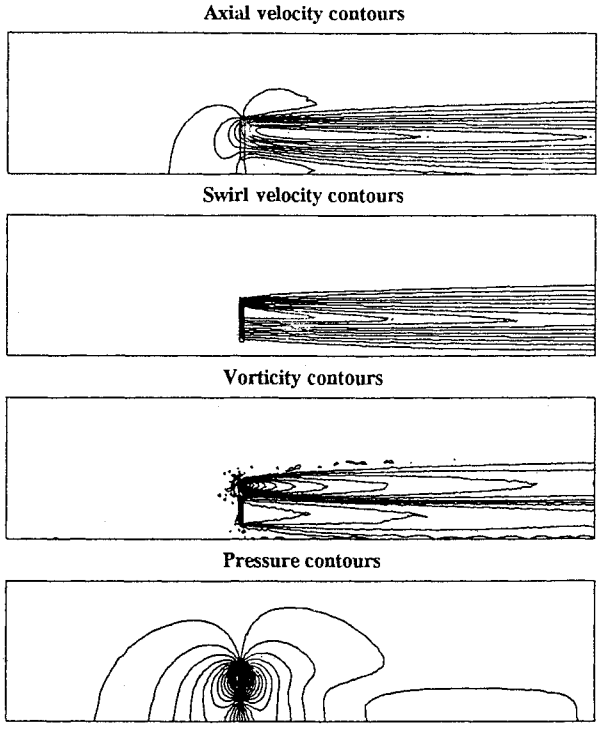

Fig. 6 Solution on final mesh.

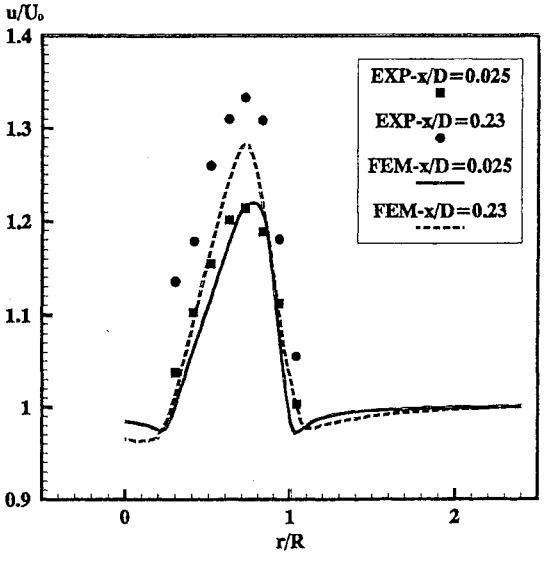

Fig. 7 Axial velocity profile.

tion that is clearly beyond the scope of this paper. Secondly, mean flow quantities are not measured with the same accuracy. For the experiment of Kotb,[16] the order of decreasing accuracy in the measurements of mean flow properties is axial velocity, pressure, swirl, and lastly, radial velocity. For the present finite element scheme, pressure is somewhat less accurately predicted than the three velocity components.

The computations were performed using both the projection and local problem error estimators. The behavior of the adaptive process is presented in Tables 3 and 4.

Both estimators produce a reduction of the error at each cycle by a factor that is very close to the requested value of 3. Hence, solution accuracy improves steadily at each adaptation cycle and reaches about 1% in relative error on the fourth mesh. Note that in both cases the meshes, solution and error norms behave similarly. Nearly identical results were obtained with both methods. Hence, only one set of results is presented.

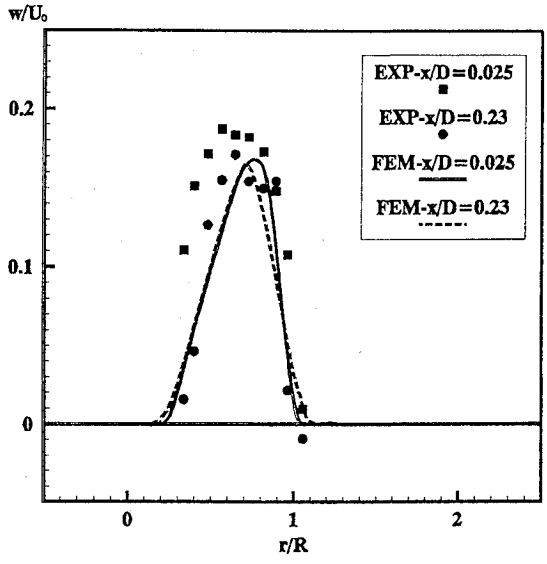

Fig. 8 Swirl profile.

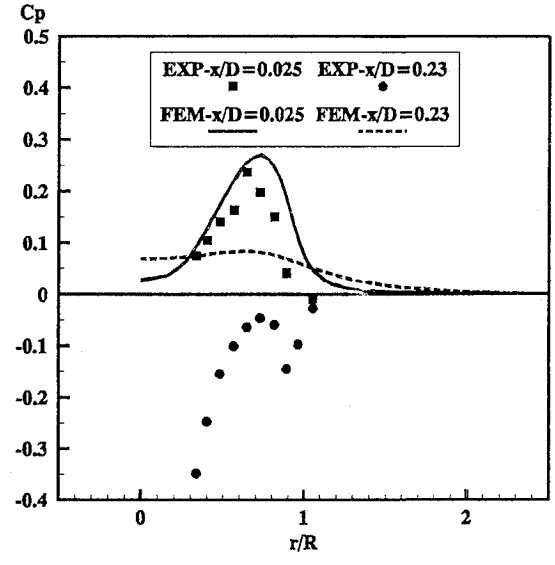

Fig. 10 Pressure distribution.

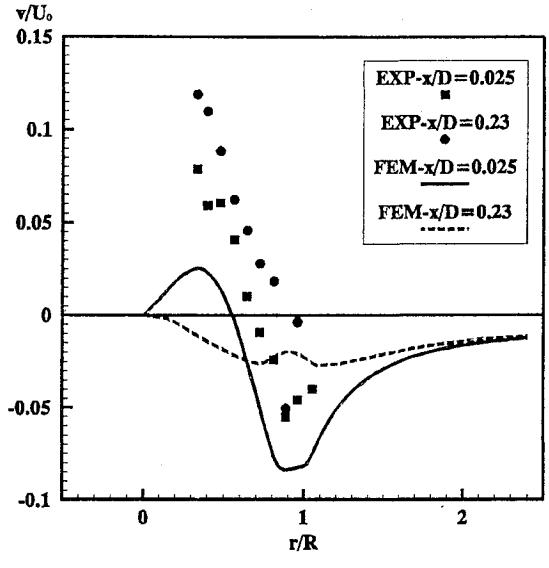

Fig. 9 Radial velocity profile.

Figure 4 presents the meshes obtained at each cycle of adaption using the projection estimator. Cycle-4 produces a grid with very high refinement near the propeller due to fluid acceleration and pressure variations. Figure 5 shows contours of pressure obtained on some of the meshes plotted in Fig. 4. As can be seen, resolution improves drastically between the initial and final mesh. The parasitic pressure field observed on the initial mesh has completely disappeared on the final grid. The contour lines of the axial and swirl velocity components, vorticity, and pressure on the final mesh are plotted in Fig. 6. Contours are crisp and smooth indicating that the mesh adequately resolves the flow.

Figure 7 compares the experimental and predicted axial velocity profiles. The agreement is excellent at $x/D = 0.025$ and good at $x/D = 0.23$. One clearly sees the acceleration of the flow downstream of the propeller. The small dip in axial velocity near the propeller tip, typical of such flows, is difficult to predict numerically, and has been previously observed both experimentally and numerically.[8,10,18] Figure 8 presents the predicted and experimental swirl profiles. Agreement between predictions and experiments is good and constitutes an improvement over those of Refs. 8 and 9. It can be seen that the assumed radial distribution of the swirling body force results in a reasonable swirl distribution. However, results indicate slightly too sharp a peak located too close to the propeller tip. This is caused by the use of Eqs. (10) for both thrust and torque distributions. Improved predictions could certainly be achieved by changing the radial distribution of torque to better match the measurements. However, there is little theory on which to base such a change. Until such theoretical foundations can be developed, adhoc changes of the torque distribution should be viewed as refining a postdictive computational capability rather than developing a predictive tool.

Figure 9 compares the predicted and measured profiles of radial velocity. The predictions display the expected shape for a free-running propeller: outward flow close to the axis and inward farther out in the freestream due to the acceleration of the fluid. This component of velocity is the most difficult to measure and is subject to the highest experimental uncertainty. At the first station ($x/D = 0.025$), the experiments display a behavior similar to that of the predictions, but the magnitudes do not agree. This could be attributed to the presence of the spinner and shaft. At the second station ($x/D = 0.23$), the experimental velocity distribution is directed outward, although that of the predictions points mostly inward. This experimental behavior is probably caused by the presence of the drive housing. Finally, Fig. 10 presents the predicted and measured radial profiles of the pressure given in the form of a pressure coefficient $C_p = 2(p^* - P_0^*)/(\rho^* U_0^{*2})$, with $P_0^* = 0$ the freestream pressure. The agreement with experiments should be considered as good at the first station ($x/D = 0.025$). At the second station, predictions are in qualitative agreement with the theory of the free-running propellers whereas experimental profiles at $x/D = 0.23$ present negative values typical of the flow over an obstacle such as the drive housing.

Computational Efficiency

Results presented in the preceding section illustrate the accuracy that can be achieved with adaptivity. The proposed strategy also results in a cost-effective solution algorithm that is well worth the added complexity. Table 5 contains computational statistics obtained on an IBM E/S 9000 with vector facility using the projection estimator. Timings include all aspects of computations (grid generation, flow solution, error estimation, and interpolation of the solution between grids).

Computation of the estimate error represents typically less than 5% of the cost of obtaining a solution on a given mesh. Complete solution of this problem required a total of 524 CPU seconds. Solving the same problem directly on the final mesh without using intermediate grids would have required approximately 800 CPU seconds. The results are not as spectacular as those observed for other laminar flows,[4-7] due to the strong nonlinearities in the diffusion terms, but the adaptive strategy still proves costeffective.

It should also be noted that without adaptivity it would have been nearly impossible to generate a grid leading to comparable accuracy without doubling the number of grid points on the final

mesh. In fact, it is very difficult to achieve a good allocation of grid points without the extra knowledge gained from the error estimates. Given that Gaussian elimination is used at each Newton iteration, the increase in computational cost is proportional to the cube of the number of grid points. It follows that nonadaptive computations of comparable accuracy would have been far more expensive than the adaptive ones.

Conclusions

An adaptive remeshing finite element procedure has been presented for solving turbulent flow past a propeller. The proposed adaptive procedure has shown to be very robust. It can be used in a nearly blackbox fashion with little or no intervention on the part of the user.

Predictions for uniform turbulent flow past a propeller show excellent agreement with the experiments for axial and swirl components of the velocity and good agreement for pressure. The adaptive remeshing procedure for turbulent flow has produced improved predictions when compared to previous work.

Acknowledgment

This work was supported by the Natural Science and Engineering Research Council of Canada.

References

[1]Peraire, J., Vahdati, M., Morgan, K., and Zienkiewicz, O. C., "Adaptive Remeshing for Compressible Flows," *Journal of Computational Physics*, Vol. 72, No. 2, 1987, pp. 449–466.

[2]Wu, J., Zhu, J. Z., Szmelter, J., and Zienkiewicz, O. C., "Error Estimation and Adaptivity in Navier-Stokes Incompressible Flows," *Computational Mechanics*, Vol. 6, No. 3, 1990, pp. 259–270.

[3]Wang, K. C., and Carey, G. F., "Adaptive Grids for Coupled Viscous Flow and Transport," *Computational Methods of Applied Mechanical Engineering*, Vol. 82, No. 4, 1990, pp. 365–383.

[4]Hétu, J. F., and Pelletier, D., "Adaptive Remeshing for Viscous Incompressible Flows," *AIAA Journal*, Vol. 30, No. 8, 1992, pp. 1986–1992.

[5]Hétu, J.-F., and Pelletier, D., "A Fast Adaptive Finite Element Scheme for Viscous Incompressible Flows," *AIAA Journal*, Vol. 30, No. 11, 1992, pp. 2677–2682.

[6]Pelletier, D., and Hétu, J.-F., "An Adaptive Finite Element Methodology for Incompressible Viscous Flows," *Advances in Finite Elements for Fluid Dynamics II*, ASME Winter Annual Meeting (Anaheim, CA), American Society of Mechanical Engineers, New York, 1992.

[7]Pelletier, D., Hétu, J.-F., and Ilinca, F., "Adaptive Finite Element Method for Thermal Flow Problems," *AIAA Journal*, Vol. 32, No. 4, 1994, pp. 741–747.

[8]Pelletier, D., and Schetz, J. A., "Finite Element Navier-Stokes Calculation of Three-Dimensional Flow Near a Propeller," *AIAA Journal*, Vol. 24, No. 9, 1986, pp. 1406–1409.

[9]Pelletier, D., and Garon, A., "Finite Element Method for Computing Turbulent Propeller Flow," *AIAA Journal*, Vol. 29, No. 1, 1991, pp. 68–75.

[10]Kotb, M. A., "Experimental Investigation of 3-D Turbulent Free Shear Flows Past Propellers and Windmills," Ph.D. Thesis, Aerospace and Ocean Engineering Dept., Virginia Polytechnical Inst. and State Univ., Blacksburg, VA, 1984.

[11]Schetz, J. A., *Injection and Mixing in Turbulent Flows*, Progress in Astronautics and Aeronautics, Vol. 68, AIAA, New York, 1981, pp. 97–122.

[12]Zienkiewicz, O. C., Gago, J. P., and Kelley, D. W., "The Hierarchical Concepts in Finite Element Analysis," *Comp. Struct.*, Vol. 16, No. 1, 1983, pp. 53–65.

[13]Lohner, R., Morgan, K., and Zienkiewicz, O. C., "Adaptive Grid Refinement for the Euler and Compressible Navier-Stokes Equations," *Accuracy Estimates and Adaptive Refinement in Finite Element Computations*, Wiley, New York, 1986.

[14]Fortin, M., and Fortin, A., "Experiments with Several Elements for Incompressible Flows," *International Journal of Numerical Methods in Fluids*, Vol. 5, No. 9, 1985, pp. 911–928.

[15]Pelletier, D., and Fortin, A., "Are FEM Solutions of Incompressible Flows Really Incompressible? (or how simple flows can cause headaches)," *International Journal of Numerical Methods in Fluids*, Vol. 9, No. 11, 1989, pp. 99–112.

[16]Zienkiewicz, O. C., and Zhu, R. J. Z., "A Simple Error estimator and Adaptive Procedure for Practical Engineering Analysis," *International Journal for Numerical Methods in Engineering*, Vol. 24, No. 3, 1987, pp. 337–357.

[17]Hétu, J. F., "Méthode d'éléments finis adaptatives pour les écoulements visqueux incompessibles," Ph.D. Thesis, Dept. of Applied Mathematics, École Polytechnique de Montréal, Montreal, Quebec, Canada, Dec. 1991.

[18]Schetz, J. A., Pelletier, D., and Mallory, D. A., "Experimental and Numerical Investigation of a Propeller with Three-Dimensional Inflow," *AIAA Journal*, Vol. 4, No. 4, 1988, pp. 341–349.